3D Sparse norm inversion of gravity and magnetic data: A case study of Gol-e-Gohar mine in Iran

Amirabbas Houshang [a] , Bardiya Sadraeifar [b], Maysam Abedi [a, *], Omid Asghari [a]

[a] *School of Mining Engineering, Faculty of Engineering, University of Tehran, Iran.*
[b] *Institute of Geophysics, University of Tehran, Iran*

ABSTRACT

This study employs a constrained mixed L_p norm inversion to assess the efficacy of geophysical potential field methods in delineating high-grade iron mineralization zones within the Gol-e-Gohar No. 2 deposit, located in the Sanandaj-Sirjan zone of southwest Iran. Given the considerable density and susceptibility contrast between iron ore, particularly the massive Kiruna-type magnetite ± apatite mineralization, and the surrounding metamorphic host rocks, extensive ground-based gravity and magnetic data were collected across a survey area spanning 1600m × 900m. To validate the effectiveness of the sparse norm inversion algorithm, two synthetic models were initially evaluated. These models included a dipping prism and two vertical prisms. Subsequently, after essential gravity and magnetic data corrections, the algorithm was applied to the acquired field data. The accurately recovered models obtained through the iterative inversion process were visually presented through four cross-sections covering the primary anomalous region, revealing a robust spatial correlation between high-density contrast and high-magnetization zones. Further development of 3D reconstructed models for density contrast and magnetic susceptibility demonstrated significant consistency with geological data obtained from exploratory boreholes, effectively delineating three distinct mineralization zones with vertical expansions ranging from 100 to 300 meters. These zones were characterized by magnetized regions enclosed within the dense rock formations.

Keywords: *Gravity data, Magnetic data, Mixed Lp norm inversion, Gol-e-Gohar iron deposit, Exploratory boreholes.*

1. Introduction

Economic iron deposits in the Earth's crust, particularly Banded Iron Formations (BIFs), Iron Oxide Copper Gold (IOCG) deposits, Iron Oxide-Apatite (IOA) deposits, and Kiruna-Type deposits, are critical mineral resources that fuel industrialization and meet global demand, playing an essential role in modern societies [1]. Fortunately, exploration of these ore deposits is facilitated by geophysical potential field methods. These techniques capitalize on the pronounced density contrast (due to dense iron minerals) and high magnetic susceptibility (owing to their ferromagnetic nature) of iron ore bodies, rendering them easily detectable through gravity and magnetic surveys. Other geophysical methods, such as seismic exploration and geoelectrical surveys (e.g., induced polarization and direct current resistivity) are not completely suitable for iron exploration due to several factors. Seismic methods, while offering high resolution and depth penetration, may struggle with the steeply dipping formations commonly found in iron ore deposits, as they have traditionally been more tailored to hydrocarbon exploration. Geoelectrical methods, while useful for lithological and structural mapping, are not as effective in directly targeting iron ore mineralization due to their lower sensitivity.

Common types for modelling iron ore deposits with geophysical potential field methods involve three main approaches: joint interpretation, cooperative inversion, and joint inversion. Joint interpretation [2, 3, 4, 5, 6], the fastest method, involves independently inverting gravity and magnetic data to obtain density contrast and susceptibility models, and then interpreting them together. Cooperative

inversion goes a step further - both datasets are inverted simultaneously, with model parameters from one influencing the other, leading to a model that best fits both datasets [7, 8, 9, 10]. This approach promotes stronger data coupling. Finally, joint inversion directly couples the data through structural or petrophysical relationships [11, 12, 13, 14, 15, 16], allowing them to influence each other during the inversion for potentially the most accurate model, but at the cost of increased computation time.

This study employs a joint interpretation approach. Initially, we derive independent density and susceptibility models through mixed L_p norm inversion of gravity and magnetic data [17, 18]. We utilize a sparse combination via a mixed norm approach to promote sparsity in the inversion results, thereby achieving a recovered model with sharper boundaries and avoiding overly smooth models [18, 19]. Subsequently, these results undergo comprehensive interpretation, integrating available geological information and borehole data for a complete analysis.

Iran encompasses three primary regions renowned for their iron mineralization potential [20]. The first region is the Khaf province, home to the Sangan mining complex, which holds an estimated 900 million tons of iron reserves [20, 21]. The second region, Bafq province, hosts several prominent deposits, including Choghart, Chadormalou, Sechahoon, Chahgaz, Nariganan, and Shavaz, collectively containing approximately 2 billion tons of iron reserves [20, 22, 23]. Finally, the third region, Sirjan province, is distinguished by the Gol-e-Gohar iron

---

* Corresponding author. *E-mail address:* maysamabedi@ut.ac.ir (M. Abedi).

deposit, which contains an estimated 1.2 billion tons of iron reserves [20, 24]. The Gol-e-Gohar complex, situated in the south of Iran, is the largest iron deposit in the Middle East. It encompasses six major mines located about 55 kilometers southwest of Sirjan city [24]. Among these, Gol-e-Gohar No.3 is the most substantial iron deposit. However, Gol-e-Gohar No.2 also holds significant iron reserves, contributing substantially to the district's overall importance in Iran's mining landscape [20].

In a review of prior geophysical investigations on the Gol-e-Gohar complex, in 2012, Ansari et al. utilized an upward continuation and Euler deconvolution method to analyze the observed gravity and magnetic anomalies [25]. Subsequently, in 2019, Behnam and Ramazi applied the power spectrum analysis and 3D modelling to interpret anomaly No. 8 [26]. Furthermore, in 2021, Milano et al. conducted a joint interpretation of gravity and magnetic data employing a 2D inversion process using a damped weighted minimum-length approach [5]. Finally, Bizhani et al. (2023) carried out a 2D inversion of magnetic data using the same methodology as the preceding study [27]. Although the mentioned research efforts were successful in identifying and modelling crucial mineralization zones, our study employs an updated and more robust inversion approach. By utilizing an expanded set of study profiles, we aim to scrutinize the targeted iron mineralization with greater precision. By using a sparse norm inversion strategy, we improve the accuracy of our iron ore modelling, achieving sharper boundaries and more precise depth estimates than previous studies. Following the inversion process, we validate our reconstructed models by comparing them with the true geological model derived from borehole data.

It is important to note that, given the nature of the Gol-e-Gohar iron deposits as Kiruna type, utilizing magnetization vector inversion and incorporating remanent magnetization would likely yield more effective results [28, 29]. This is recommended for future studies on this extensive iron deposit. However, while susceptibility inversion disregards remanent magnetization and focuses on induced magnetization, it remains an acceptable method for primary inverse modelling.

The subsequent sections of this article are structured as follows. Prior to presenting the physical properties derived from geophysical data, a brief exposition is provided on the methodology encompassing forward and inverse modelling, synthetic scenarios, and the geological setting. Each segment of our results model is thoroughly described, featuring a comparative analysis of proposed exploration targets with existing borehole data and geological evaluations. The final section offers a comprehensive summary of the overall findings from this research. Geophysical modelling was executed using the SimPEG package (version 0.20.0) via the Python programming language [30]. The hardware configuration utilized for both forward and inverse modelling consists of an ASUS laptop equipped with an AMD A6 2.4 GHz CPU and 8 GB of RAM.

2. Methodology

In this section, we first discuss the mathematics of gravity and magnetic forward modelling. Next, we provide a detailed examination of the mixed norm inversion approach for the independent inversion of gravity and magnetic data.

2.1. Forward modelling

Solving the forward problem allows us to predict geophysical datasets that correspond to particular subsurface geological structures. In essence, through the utilization of model parameters ($\mathbf{c}$) as an example, we can predict the resultant data ($\mathbf{d}$), utilizing A_s as the mathematical operator for forward modelling connected to the causative source $\mathbf{s}$ [31]:

$$\mathbf{d} = A_s(\mathbf{c}). \tag{1}$$

In the context of gravity forward modelling, first we define the gravity vector ($\mathbf{g}$), containing components in the x, y, and z directions (Eq. 2). These components are related to the density distribution through the

tensor T. This tensor essentially translates the density value at each cell (ρ) into the gravitational field observed at a specific location, P (x_P, y_P, z_P) [32].

$$\mathbf{g} = \begin{bmatrix} T_x \\ T_y \\ T_z \end{bmatrix} \rho. \tag{2}$$

Most gravity forward modelling studies primarily utilize the vertical component of the gravity field (g_z) due to its superior ability to detect variations in subsurface density distribution [33]. Eq. (3) defines this component [33, 34]:

$$g_z = T_z \rho. \tag{3}$$

The specification of T_z is outlined in Eq. (4):

$$T_z = -G^* \left(arctan \frac{dxdy}{rdz} + log[dy + r] + log[dy + r] \right) \Big|_{x_L}^{x_U} \Big|_{y_L}^{y_U} \Big|_{z_L}^{z_U},$$
$$r = (dx^2 + dy^2 + dz^2)^{1/2},$$
$$dx = (x_p - x), dy = (y_p - y), dz = (z_p - z). \tag{4}$$

In each unit cell, establishing the relative distance $r(dx, dy, dz)$ between the observation point and the nodal boundaries requires solely the coordinates of the lower southwest corner $L(x_L, y_L, z_L)$ and the upper northeast corner, identified as $U(x_U, y_U, z_U)$. In situations involving a considerable quantity of observation points, the primary equation utilized for gravity forward modelling calculations is denoted by Eq. (5) [33]:

$$\mathbf{g}^{pre} = \mathbf{F}_G \rho. \tag{5}$$

In the equation provided, $\mathbf{F}_G$ represents the forward operator matrix used in gravity modelling. It transforms the space of physical parameters into the data space denoted as $\mathbf{g}^{pre}$, where $\rho \in R^M$, $\mathbf{g}^{pre} \in R^N$, $\mathbf{F}_G \in R^{N \times M}$. Here, M signifies the total number of cells, and N indicates the number of observation points [33, 34].

For magnetic forward modelling [33, 35], we start by defining the forward problem analogous to Eq. (2). This linear system is expressed in Eq. (6), where $\mathbf{S}$ represents a symmetric matrix that describes the linear relationship between a prism with magnetization $\mathbf{m}^* = [M_x, M_y, M_z]^S$ and the magnetic field components $\mathbf{b} = [b_x, b_y, b_z]^S$.

$$\mathbf{b} = \mathbf{S}\mathbf{m}^*. \tag{6}$$

The tensor $\mathbf{S}$, detailed in Eq. (7), is a symmetric matrix with a zero trace. Its components are $S_{xx}, S_{xy}, S_{xz}, S_{yy}, S_{zy}, S_{zz}$.

$$\mathbf{S} = \frac{\mu_0}{4\pi} \begin{bmatrix} S_{xx} & S_{xy} & S_{xz} \\ S_{xy} & S_{yy} & S_{zy} \\ S_{xz} & S_{yz} & S_{zz} \end{bmatrix}. \tag{7}$$

Finally, we can formulate the magnetic forward modelling equation analogous to Eq. (5), as shown in Eq. (8). Here, $\mathbf{F}_T$ is the forward operator matrix for magnetic modelling, with $\mathbf{m}^* \in R^{3M}$, $\mathbf{b}^{pre} \in R^N$, $\mathbf{F}_T \in R^{N \times 3M}$ [33, 35].

$$\mathbf{b}^{pre} = \mathbf{F}_T \mathbf{m}^*. \tag{8}$$

2.2. Inverse modelling

The theoretical foundation for the inversion methodology employed within the SimPEG framework is laid out in the pioneering works of Li and Oldenberg (1996, 1998) [36, 37]. Subsequently, Fournier et al. (2016, 2019) introduced a more advanced and robust framework for this approach [17, 18]. This inversion method is typically based on minimizing an objective function, which is classified as an optimization problem and formulated as follows:

$$\min \phi(m) = \phi_d + \beta \phi_m. \tag{9}$$

In Eq. (9), (m) denotes the objective function to be minimized through the iterative inversion process. The component ϕ_d represents the data misfit term, ensuring that the recovered model accurately

predicts the field observations (gravity and magnetic data). The component ϕ_m is the model objective function or regularization function, which ensures the recovered model reflects plausible geological features and exploration targets. Lastly, the parameter β balances the relative contributions of ϕ_d and ϕ_m within the final objective function ($\phi(m)$)[36, 37]. The misfit function expressed in Eq. (10) quantifies the disparity between observed data (d^{obs}) and predicted data (d^{pred}) and σ represents the estimated uncertainties in the data [36, 37, 38].

$$\phi_d = \sum_{i=1}^N \left(\frac{d_i^{pred} - d_i^{obs}}{\sigma_i}\right)^2 \tag{10}$$

The regularization function (ϕ_m) introduces prior information and constraints to the inverse problem, mitigating its inherent non-uniqueness. The most frequently used approach employs the L_2-norm measure, leading to a discrete linear system as shown in Eq. (11):

$$\phi_m = \alpha_s\phi_s + \alpha_x\phi_x + \alpha_y\phi_y + \alpha_z\phi_z = \sum_{r=s,x,y,z} \alpha_r \|W_r V_r G_r (m - m^{ref})\|_2^2 \tag{2}$$

In Eq. (11), the term ϕ_s measures the deviation of the discrete model (m) from a reference model (m^{ref}) and ϕ_x, ϕ_y, and ϕ_z assess the roughness of the model in the respective x, y, and z directions. The coefficients α_s, α_x, α_y, and α_z regulate the closeness of the derived model to the reference model and control the smoothness of the resulting model, respectively [36, 37, 38]. The matrices G_x, G_y, and G_z represent discrete gradient operators, which are used to calculate the model gradients in different directions [36, 37]. For the smallness component, G_s reduces to the identity matrix, indicating that it does not contribute to the gradient computation. The term W_s represents the weight associated with the smallest model component, ensuring that the smallest possible model is favored. Similarly, W_x, W_y and W_z are weights that correspond to the flatness of the model in the x, y, and z directions, promoting smooth transitions in the model across these axes. W_m is the combined weighting matrix that integrates all these weights, providing a balanced approach to both model adherence to the reference and its smoothness across all dimensions. This comprehensive weighting scheme ensures that the derived model is both physically plausible and smooth, adhering to the constraints and prior information provided [36, 37, 38].

In the mixed L_p-norm condition, the regularization term can be written as follows [18]:

$$\phi_m^p = \alpha_s \|V_s R_s m\|_2^2 + \sum_{r=x,y,z} \alpha_r \|V_r R_r D_r m\|_2^2 \tag{12}$$

Where G_r is substituted with the finite difference operator D_r as represented below [18, 33]:

$$D_r = \begin{bmatrix} -1 & 1 & 0 & \dots & 0 \\ 0 & \ddots & \ddots & \ddots & \vdots \\ \vdots & \ddots & 0 & -1 & 1 \end{bmatrix} \tag{13}$$

We utilize a scaled iterative reweighted least squares method (S-IRLS) to tackle a sequence of weighted least squares problems iteratively. The computation of the IRLS weight (R_r) is outlined below [18, 33]:

$$R_r = diag\left[\left(\epsilon_r^2 + \left(D_r m^{(k-1)}\right)^2\right)^{\frac{p_r}{2}-1}\right]^{\frac{1}{2}} \tag{14}$$

In the provided equation, ϵ stands for the threshold parameter, $m^{(k-1)}$ represents the model obtained from the preceding iteration, and V_r (Eq.12) signifies the volume terms linked with the discretization. Additionally, p_r denotes the regularization parameter linked with the r-th direction (e.g., x, y, or z). Through iterative updates of these weights, the Iterative Reweighted Least Squares (IRLS) method facilitates the convergence of the inversion process toward a solution that effectively balances the fit to the observed data and adheres to the regularization constraints [33]. The final objective function for the mixed-norm inversion of gravity and magnetic data is described as follows, where the

symbol κ denotes the magnetic susceptibility, reflecting our adoption of susceptibility inversion and ρ represents the density contrast through the gravity inversion:

$$\min \phi(m)_{grav} = \|F_G \rho - d_{grav}{}^{obs}\|_2^2 + \beta(\alpha_s\|V_s R_s m_\rho\|_2^2 + \sum_{r=x,y,z} \alpha_r \|V_r R_r D_r m_\rho\|_2^2),$$

$$\min \phi(m)_{mag} = \|F_b \kappa - d_{mag}{}^{obs}\|_2^2 + \beta(\alpha_s\|V_s R_s m_\kappa\|_2^2 + \sum_{r=x,y,z} \alpha_r \|V_r R_r D_r m_\kappa\|_2^2). \tag{15}$$

3. Synthetic scenarios

This section assesses the effectiveness of the mixed-norm inversion method in recovering two synthetic models. The first model, a dipping prism, investigates the method's ability to differentiate between the recovery of deeper and shallower sections of a dipping structure. This evaluation is critical for understanding the inversion's capability for reconstructing features at depth and its sensitivity to structures with gentle dips. The second model, comprised of vertical prisms, examines the method's ability to resolve and distinguish separate causative sources. Here, we assess its proficiency in recovering vertical structures located at varying depths.

To efficiently represent the subsurface environment, we employ tree meshes [30]. These adaptable grids allow us to define a refined box with smaller cells concentrated around the area of interest. This targeted refinement focuses computational power on the structures we aim to recover (causative sources) while reducing the number of cells in less critical areas. This approach leads to a potential improvement in the accuracy of recovered features and a significant reduction in computational time compared to using a uniform mesh size across the entire domain.

3.1. Dipping prism

The first synthetic model (Fig.1) represents a dipping prism with a density contrast of 1.0 g/cm³ and a magnetic susceptibility of 0.3 SI without remanent magnetization. This prism consists of five rectangular slabs with dimensions of 70m × 50m × 20m. To improve resolution in the target area, a refined box with smaller cells is implemented. This box extends from -130m to 130m in the x-direction, -80m to 80m in the y-direction, and -10m to -130m in the z-direction. The entire synthetic survey area encompasses a 320m × 320m × 160m environment, with x and y ranging from -160m to 160m and z ranging from 0 to -160m. The spacing of the observation points is about 20 m, and there are a total of 256 points (in both synthetic models).

In the construction of both synthetic models, a flat topography was adopted for two primary reasons. Firstly, synthetic modelling often seeks to simulate idealized geometric shapes that approximate the key features of the target anomaly. Since the real-world case study exhibits a relatively smooth topography, neglecting it simplifies the synthetic model and allows us to isolate the performance of the sparse norm inversion algorithm. Secondly, employing a flat topography in both synthetic models ensures that the inversion results are primarily influenced by the causative sources and not by additional complexities arising from topographic variations.

Fig.2 depicts the inversion results in an Easting-Elevation cross-section, showcasing the density contrast and susceptibility models (Figs. 2a and 2b) obtained after 20 iterations through the mixed L_p norm inversion. This approach utilizes a customizable norm combination denoted as $[p_s, p_x, p_y, p_z]$, where $0 \leq p \leq 2$. The first norm (p_s), referred to as the model norm, applied to both density contrast and susceptibility models, controls sparsity [39]. In this case, we use the L_0 norm ($p_s = 0$) to promote a model with many zero values, sharpening the distinction between the target anomaly and the background while facilitating a more effective background recovery [18, 33, 39]. The

remaining L_2 norms are applied to the gradients of the models ($p_x = p_y = p_z = 2$), encouraging smoothness in the final recovered solution in three dimensions. This specific norm combination, $[p_s = 0, p_x = 2, p_y = 2, p_z = 2]$, is known as a sparse norm combination. Fig.2 demonstrates the successful recovery of the dipping prism through sparse norm inversion of gravity and magnetic data. This highlights the effectiveness of this approach in capturing such complex structures.
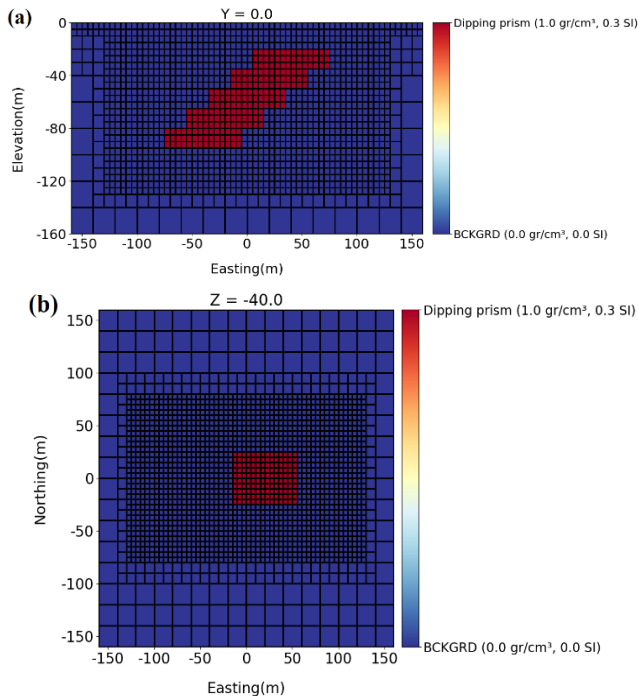

Figure 1. The first synthetic model (dipping prism) is presented in cross-sections. (a) x-z vertical cross-section at y = 0, and (b) x-y horizontal cross-section at z = -40 m.
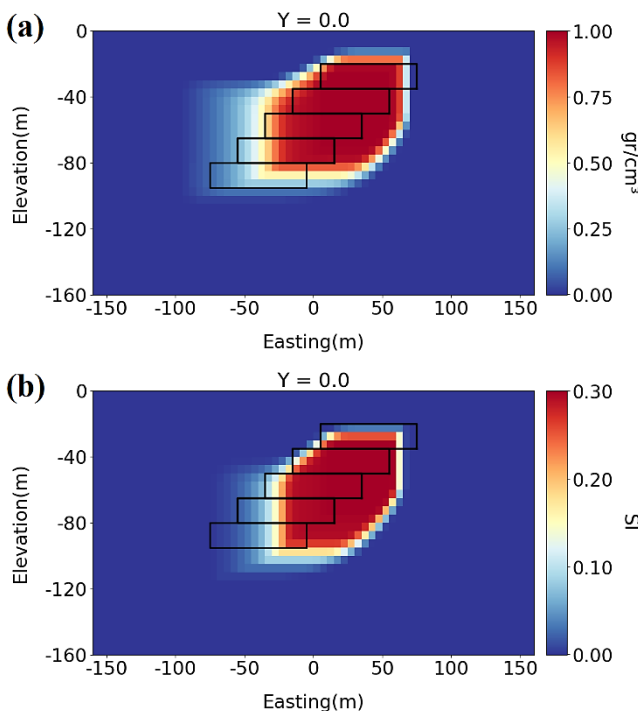

Figure 2. Inversion results for the first synthetic model along y = 0. (a) Density contrast model obtained from sparse norm inversion of gravity data, and (b) Susceptibility model obtained from sparse norm inversion of magnetic data.

Figs. 3a and 3d show the gravity and magnetic anomalies generated from the synthetic model, incorporating 5% Gaussian noise. For a simpler analysis of the observed and predicted magnetic anomalies, inclination and declination angles were set to 90° and 0°, respectively for both synthetic models and the Earth's magnetic field intensity was considered as 50000 nT. Figs. 3b and 3e display the recovered gravity and magnetic anomalies after sparse norm inversion. Finally, Figs. 3c and 3f illustrate the residual plots, representing the difference between the observed and calculated data normalized by the standard error. In simpler terms, these plots depict the discrepancy between the anomalies arising from the true and recovered models. Positive values in the residual plots indicate areas where the true model has a higher gravity or magnetic anomaly compared to the recovered model, and vice versa for negative values. It is evident that the gravity inversion was slightly more successful in recovering the true model anomaly. The acceptable normalized residuals achieved by both recovered models strongly support the effectiveness of the sparse norm inversion algorithm in reconstructing the dipping prism.

3.2. Vertical prisms

The second synthetic model (Fig.4) consists of two vertical prisms, each with a density contrast of 1.2 g/cm³ and a magnetic susceptibility of 0.4 SI without remanent magnetization. The prisms have dimensions of 30m × 40m × 70m, and one prism is positioned 20 meters deeper than the other. To improve resolution in the target area, a refined box is implemented. This box extends from -120m to 120m in both the x and y directions, and from -10m to 140m in the z-direction. The overall dimensions of the synthetic environment remain identical to the first model.

Fig. 5 displays the recovered models for the second synthetic model in an Easting-Northing cross-section after sparse norm inversion. While both density contrast and susceptibility models successfully captured the presence of the two vertical prisms, the magnetic inversion (Fig.5b) appears to be more effective in resolving the deeper portion of these structures. Similar to the first synthetic model, the recovered models were obtained after 20 iterations.

Figs. 6a and 6d display the gravity and magnetic anomalies generated from the second synthetic model, incorporating 5% Gaussian noise similar to the first model. Figs. 6b and 6e illustrate the recovered anomalies after sparse inversion, which closely resemble the true model anomalies. The normalized residuals are shown in Figs. 6c and 6f. As previously mentioned, these residuals are a valuable metric for evaluating the inversion's effectiveness in minimizing the difference between the observed and predicted data. They represent the difference between the observed and calculated data normalized by the standard error, and therefore, are unitless. In this case, the low normalized residuals for both recovered models indicate good consistency with the true synthetic model.

This section showcases the effectiveness of sparse norm inversion in recovering complex subsurface structures. The method successfully retrieves both density contrast and susceptibility models, demonstrating good sensitivity to deeper features, a known challenge for many geophysical techniques. This capability is further supported by the low residual plots, indicating a strong fit between observed and predicted data. Even with the added challenge of 5% Gaussian random noise, the sparse norm inversion method successfully handled it, highlighting its robustness. In the next section, we will evaluate this method's effectiveness in a practical geological setting by applying it to the real-world case of the Gol-e-Gohar iron deposit.

4. Application to the field data

This section applies the sparse norm inversion method to analyze field data acquired from the Gol-e-Gohar mine. We begin by providing a detailed overview of the study area's geological setting. Subsequently, we discuss the geophysical survey employed for data collection. Finally, the inversion results obtained along the study profiles are presented and analyzed.
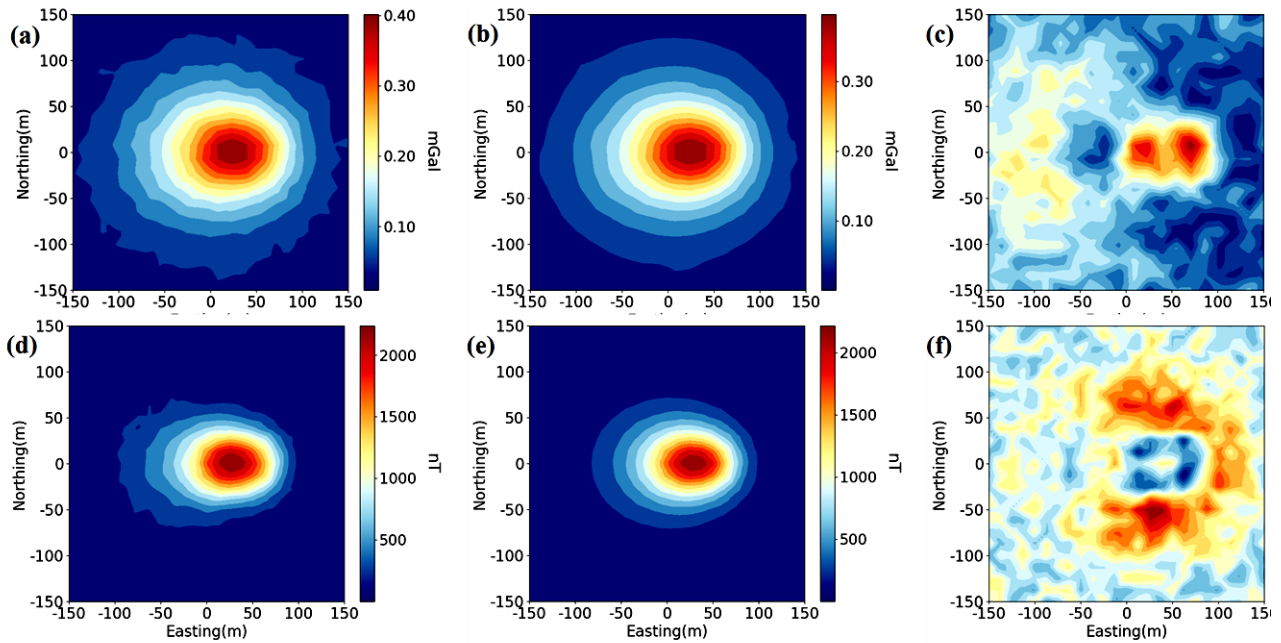
Figure 3. Resulted gravity and magnetic anomalies from true and recovered model along a horizontal cross-section (a) Gravity anomaly of the true model, (b) Gravity anomaly of the recovered model after sparse norm inversion, (c) Normalized residual for the gravity inversion, (d) Magnetic anomaly of the true model, (e) Magnetic anomaly of the recovered model after sparse norm inversion, (f) Normalized residual for the magnetic inversion.
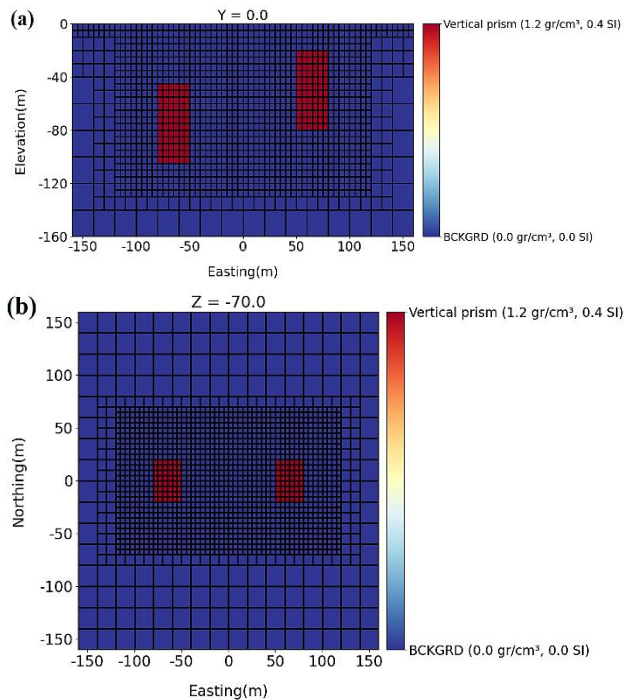

Figure 4. The second synthetic model (vertical prisms) is presented in cross-sections. (a) x-z vertical cross-section at y = 0, and (b) x-y horizontal cross-section at z = -70 m.

4.1. Geological setting

Geologically, the Gol-e-Gohar iron ore district lies entirely within the southern section of the Sanandaj-Sirjan zone (Fig.7) [40]. This zone, a narrow strip trending northwest-southeast, stretches for approximately 1500 km from western Lake Urmia to the eastern part of Bandar Abbas province in southwestern central Iran [41]. Notably, the Sanandaj-Sirjan Zone (SSZ) is situated northeast of the Zagros fold-and-thrust belt.

Having undergone extensive metamorphism, magmatism, and multiple tectonic events, this zone is considered the most tectonically unstable region in Iran [40, 41]. Due to its complex geological history characterized by numerous transformations, reliable dating and correlation of geological units pose significant challenges [41].
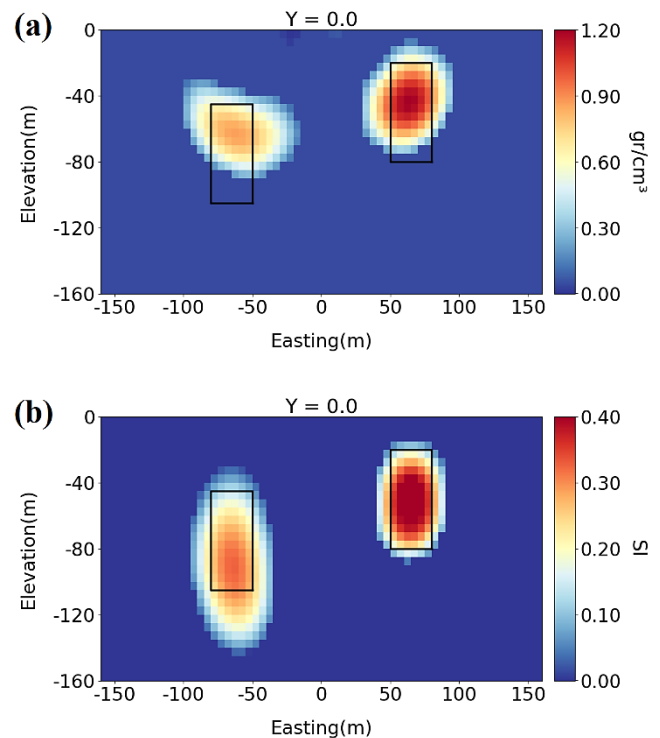

Figure 5. Inversion results for the second synthetic model along y = 0. (a) Density contrast model obtained from sparse norm inversion of gravity data, and (b) Susceptibility model obtained from sparse norm inversion of magnetic data.
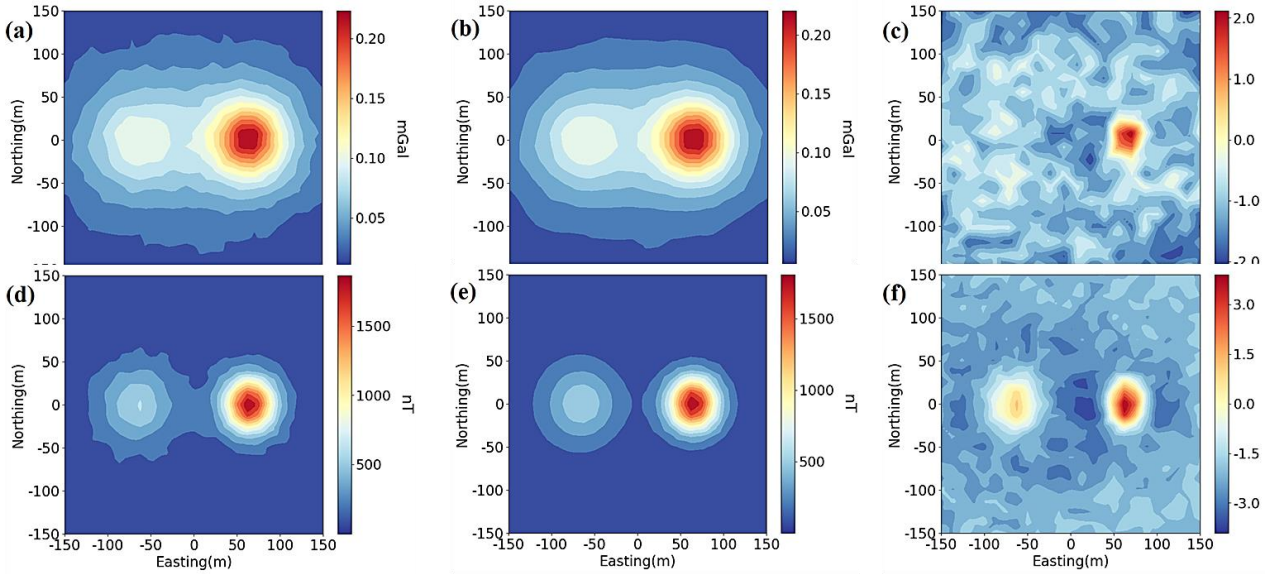
Figure 6. Resulted gravity and magnetic anomalies from true and recovered model along a horizontal cross-section. (a) Gravity anomaly of the true model, (b) Gravity anomaly of the recovered model after sparse norm inversion, (c) Normalized residual for the gravity inversion, (d) Magnetic anomaly of the true model, (e) Magnetic anomaly of the recovered model after sparse norm inversion, (f) Normalized residual for the magnetic inversion.
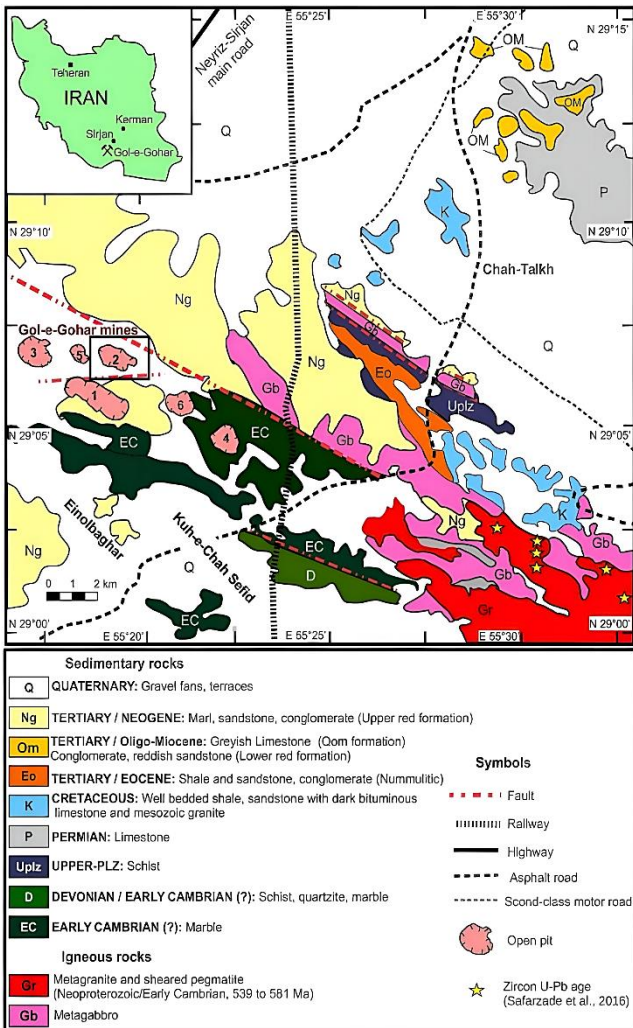

Figure 7. Geological map of the Gol-e-Gohar iron ore complex, located in the southern part of the Sanandaj-Sirjan zone. Exactly inserted with permission from [40].

The Gol-e-Gohar complex is predominantly covered by recent alluvium, obscuring most of the underlying bedrock [42]. Limited outcrops reveal Paleozoic metamorphic rocks in the south and southwest, belonging to the Gol-e-Gohar complex – the oldest metamorphic unit in the region. Mesozoic and Cenozoic sedimentary rocks are present in the eastern part of the area [42]. Its lower section consists of a sequence of gneisses, mica schists, amphibolites, and quartz schists. This sequence is overlain by another sequence comprising dolomite marble, mica schists, green schists, and graphite schists [42, 43]. The uppermost unit is composed of dolomite or calcite marble. The oldest exposed unit within the Gol-e-Gohar complex is a granite-gneiss unit with interlayers of schist and amphibolite [43]. The uranium-lead method has dated the protolith of these gneisses to be approximately 520 million years old. Metamorphic carbonate units, the youngest component of the Gol-e-Gohar complex, outcrop in various locations across the region [40]. Many researchers attribute the age of metamorphism within the Sanandaj-Sirjan zone to the Mesozoic, suggesting it resulted from the subduction of the young Tethys oceanic crust beneath the central Iranian plate [44].

Six iron ore bodies were discovered within the Gol-e-Gohar iron ore district through magnetic surveys (Fig. 7) [40, 44]. These discoveries were first made by the Iran Barite Mining Company in 1969 [45]. Outcrops in mine 2 (the study area, depicted by a black box in Fig. 7) reveal the evidence of alteration in the upper portion of the iron ore deposit [45]. This alteration, known as advanced martitization, is caused by the reaction between atmospheric water and the original iron minerals. As a result of this process, hematite forms along the edges and grain boundaries of the mineral [42, 45]. Hematite, the oxide portion, is characterized by very low sulfur content due to leaching during alteration. The color of the altered zone varies from red to brown, with some marginal areas exhibiting a yellow coloration due to the presence of limonite [45]. This type of alteration is observed down to a depth of approximately 90 meters. Below 90 meters, the iron ore transitions from hematite to black magnetite (the findings from the inversion results are consistent with this fact). The presence of pyrite veins within the magnetite indicates varying sulfur content. These magnetites can be further classified into two types based on their sulfur content: low sulfur magnetite (LSM) and high sulfur magnetite (HSM), as represented in Fig. 14a [45].

The primary iron mineralization in mine 2 is magnetite, often accompanied by pyrite in various forms [40, 45]. Additionally, minerals, such as talc, muscovite, serpentine, and occasional calcite veins are

present. A clear correlation is observed in samples between the abundance of these minerals and a decrease in both ore grade (iron content) and rock strength [42, 45]. The presence of these minerals as fracture fillings can even lead to mine instability and collapse. Furthermore, the presence of thin streaks of the host rock (mainly mica schists) within the ore body creates difficulties during extraction [44]. These intermixed materials are sometimes impossible to separate effectively. Overall, the most valuable component of the ore deposit is magnetite with low pyrite content, followed by the oxide zone (hematite). Iron-bearing schists represent the least valuable portion and fortunately, constitute a minor fraction of the total ore mass [45].

4.2. Geophysical survey

To conduct exploratory operations in the Gol-e-Gohar area, Aeroservice Company initially performed airborne geophysical surveys (magnetometry) over an expanse of 4,500 km² between Abadeh Fars and Jazmurian [45]. These surveys identified substantial iron ore deposits with high potential, exhibiting suitable grades and reserves. After the

airborne surveys, the Yugoslavian Geological Institute performed ground-based gravity and magnetic surveys over a 74 km² region in Gol-e-Gohar. These efforts culminated in the discovery of six iron ore mines within the Gol-e-Gohar complex, with mine No. 2 being one of the identified sites [45]. The geophysical dataset acquired along the Gol-e-Gohar mine No. 2 comprises 995 gravity and magnetic data points (Fig. 8). The data spacing exhibits a strategic reduction in proximity to the target regions. The maximum spacing between data points is approximately 80 meters, while the minimum spacing is around 40 meters.

Following geophysical surveys, essential gravity, and magnetic data corrections were implemented. Gravity data underwent free-air, Bouguer, topographic, and trend corrections (using a first-order polynomial fitting method) [46]. Magnetic data processing involved diurnal correction, IGRF subtraction, reduction to the pole, and trend correction to obtain residual anomalies (Figs. 8a and 8b). Inclination and declination angles in the study area were 90° and 0°, respectively and the Earth's magnetic field intensity was 45300 nT.
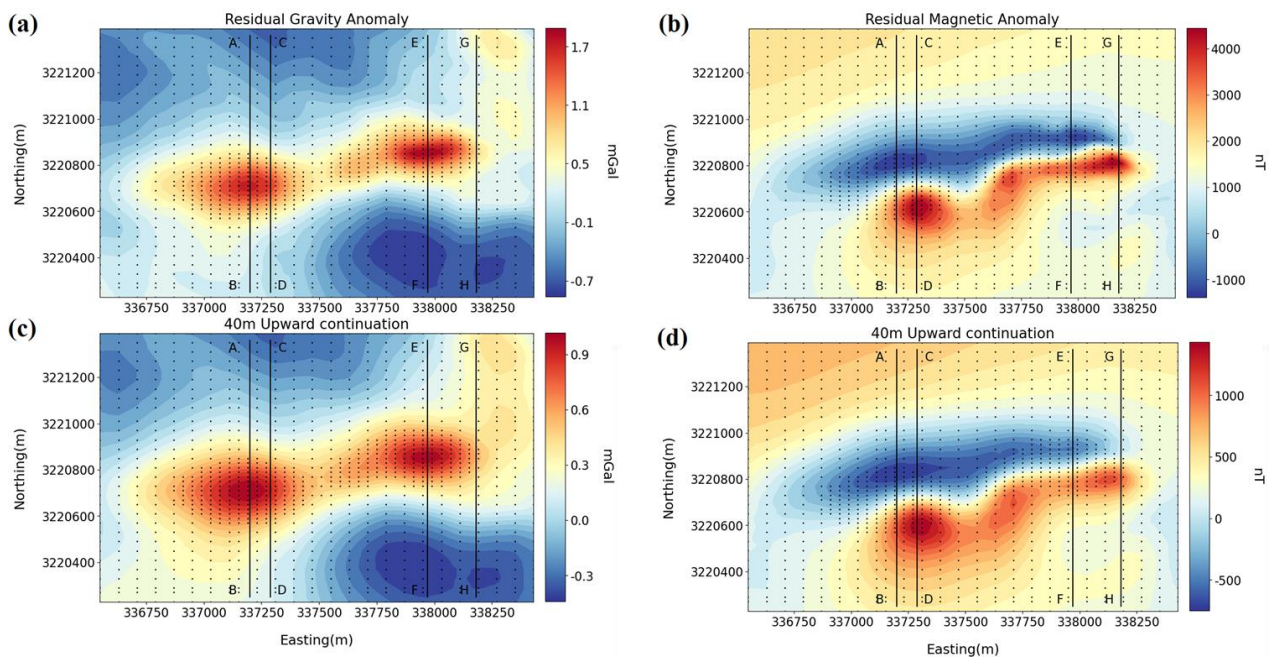

Figure 8. Processed geophysical data for the Gol-e-Gohar iron ore complex. (a) Residual gravity anomaly after applying free-air, Bouguer, topographic and trend corrections, (b) Residual magnetic anomaly after applying diurnal correction, IGRF subtraction, reduction to the pole and trend correction, (c) Gravity anomalies after 40-meter upward continuation, (d) Magnetic anomalies after 40-meter upward continuation.

After obtaining residual gravity and magnetic data, upward continuation (40 meters) was applied to both datasets (Figs. 8c and 8d), revealing minimal source location changes but slight modifications in anomaly patterns, suggesting a near-surface, dense, and magnetized ore deposit. Additionally, Fig. 8 displays study profile locations. Inversion results for four cross-sections (A-B & E-F perpendicular to the strongest gravity anomalies; C-D & G-H perpendicular to the strongest magnetic anomalies) are presented, providing valuable insights into the subsurface distribution of dense and magnetized regions. Fig. 9 presents a topographic map of the study area. The elevation variation within the survey area is approximately 16 meters, indicating a relatively flat topography. A slight but inconsequential elevation increase can be observed towards the eastern portion of the area (refer to the right side of Fig. 9).

4.3. Inversion results

After implementing data corrections, we conducted a sparse norm inversion through a mixed norm approach, as outlined in the methodology section. The inversion process was subject to specific
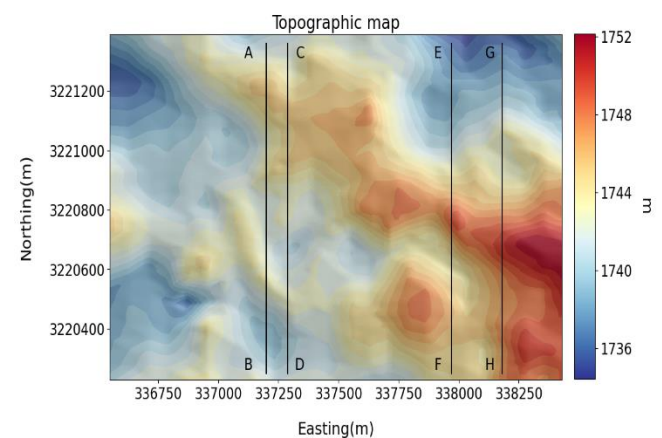

Figure 9. Topographical map of the study area with study profiles. The difference between the maximum and minimum elevation is about 16 meters, indicating that the study area has relatively smooth topography.

upper and lower constraints. For magnetic inversion, the upper limit was established at 1.0 SI based on the susceptibility assessments derived from the core samples and drilling data, with the lower limit set at 0 SI. Regarding gravity inversion, the upper constraint was defined as 1.5 g/cm³, while the lower bound was set to -0.5 g/cm³. These upper and lower bounds delineate the maximum and minimum density contrasts accommodated by the inversion algorithm. Their selection resulted from a comprehensive examination of geological and borehole data to ensure the consistency of inversion outcomes with actual geological conditions. The resultant models, encompassing density contrasts and susceptibility, were derived after 28 iterations, indicating the algorithm's attainment of the predefined target misfit.

In Figs. 10 and 11, we present the inversion results along four profiles. Figs. 10a and 10b depict density contrast and susceptibility models along the A-B profile, which crosses the high gravity anomaly region. The density contrast model (Fig. 10a) illustrates a high contrast region with a vertical distribution of 300m and a lateral distribution of 200m. The susceptibility model (Fig. 10b) delineates a magnetized region situated approximately 90-100m deeper than the high-density contrast region. This distinction between hematite and magnetite distributions was outlined in the geological report of the study area [45] and corroborated by the inversion results. Figs. 10c and 10d showcase the inversion outcomes along the C-D profile, which crosses a high magnetic anomaly.
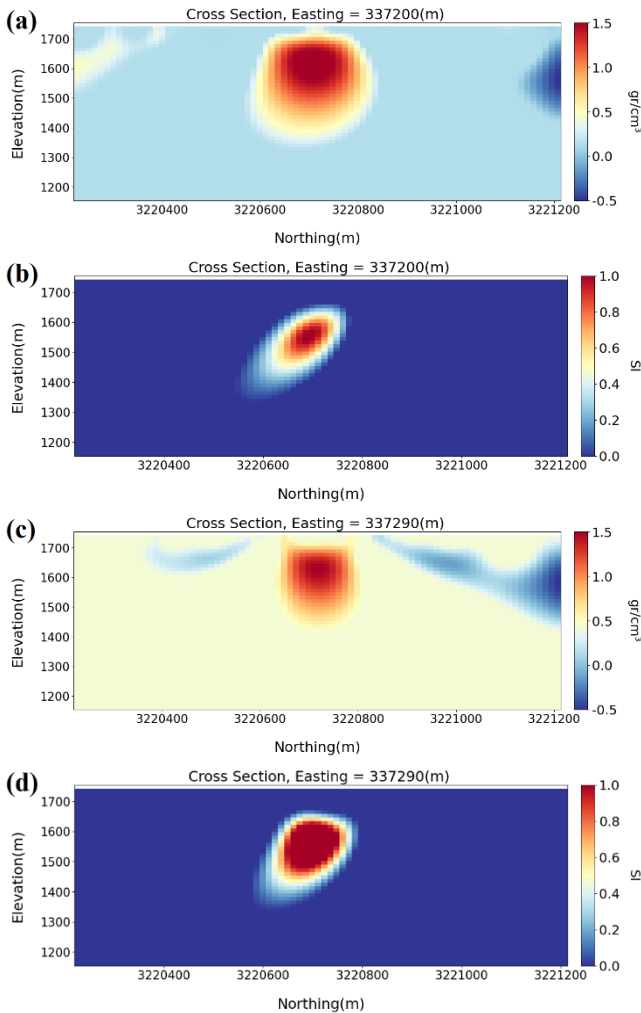
As anticipated, the inversion findings disclose a significant magnetized region with a vertical expansion of about 200m (Fig. 10d) and a high-density contrast region located approximately 70-80m higher (Fig. 10c). Fig. 10d illustrates the most extensive distribution of magnetite in the whole area. It is evident that the depth and size of the magnetized mass decrease in profiles E-F and G-H (Fig. 11).

Fig. 11a illustrates the density contrast model along the E-F profile, intersecting a significant gravity anomaly. A large, near-surface hematite ore body is clearly visible. Fig. 11b shows the susceptibility model along the same profile, indicating magnetite mineralization.

Comparing Figs. 10 and 11 reveals that, moving rightward across the survey area, both hematite and magnetite mineralizations become more superficial and increasingly overlap. In Fig. 10, high-density contrast and magnetized regions differ vertically by about 70-100 meters, but in Fig. 11 dense and magnetized masses are located at similar depths. Finally, Fig. 11c and 11d present density contrast and susceptibility models along the G-H profile, which intersects a major magnetic anomaly. Fig. 11d shows a more intensely magnetized body compared to Fig. 11b. Fig. 12 shows the normalized residuals or misfit for gravity and magnetic inversion, as discussed in the synthetic scenarios section. This plot is a useful metric for evaluating the success of the inversion in minimizing the objective function and how well the inverse model matches the true anomalies.
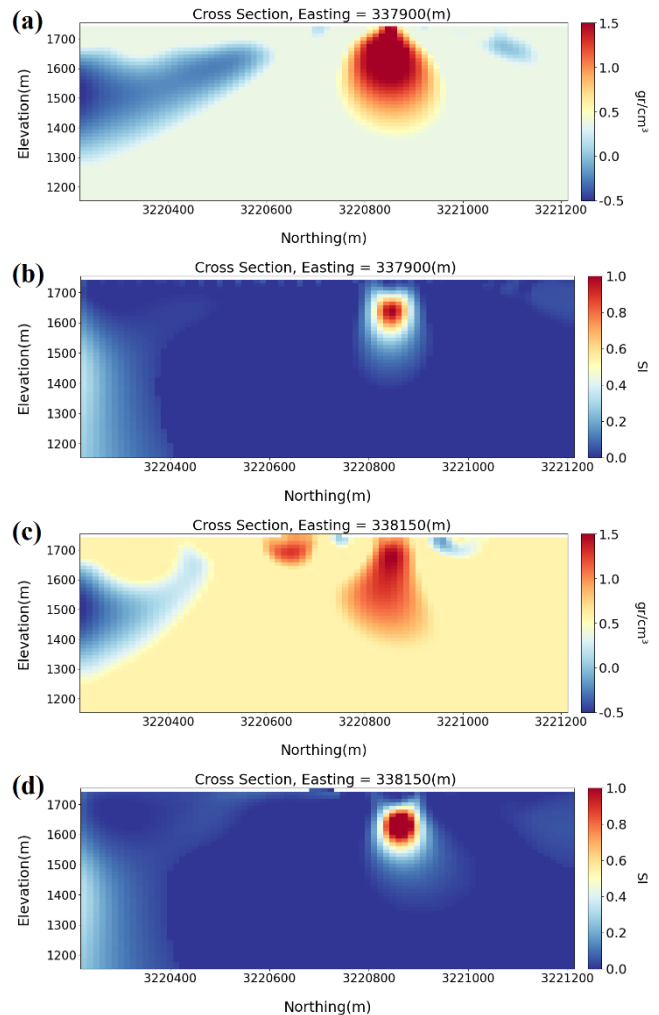

Figure 10. Inversion results along profiles A-B and C-D. (a) Density contrast model obtained along profile A-B, (b) Susceptibility model obtained along profile A-B, (c) Density contrast model obtained along profile C-D, (e) Susceptibility model obtained along profile C-D.

Figure 11. Inversion results along profiles E-F and G-H. (a) Density contrast model obtained along profile E-F, (b) Susceptibility model obtained along profile E-F, (c) Density contrast model obtained along profile G-H, (e) Susceptibility model obtained along profile G-H.

Fig. 13 shows the convergence plot, examining changes in the misfit (ϕ_d) and model parameter (ϕ_m) after each iteration during the inversion process. In this context, a decreasing trend in ϕ_d indicates that the inversion algorithm is improving the fit of the model to the observed data. Ideally, ϕ_d should decrease and converge to a minimum value as the inversion progresses. If ϕ_d stabilizes at a low value, it suggests that the model adequately explains the observed data. Concurrently, an increasing ϕ_m observed during inversion signals the ascendance of the sparsity constraint. This trend indicates a stronger imposition of simplicity on the model as the inversion proceeds. Specifically, Fig. 13a corresponds to the convergence plot for gravity inversion, and Fig. 13b portrays the convergence plot for magnetic inversion.
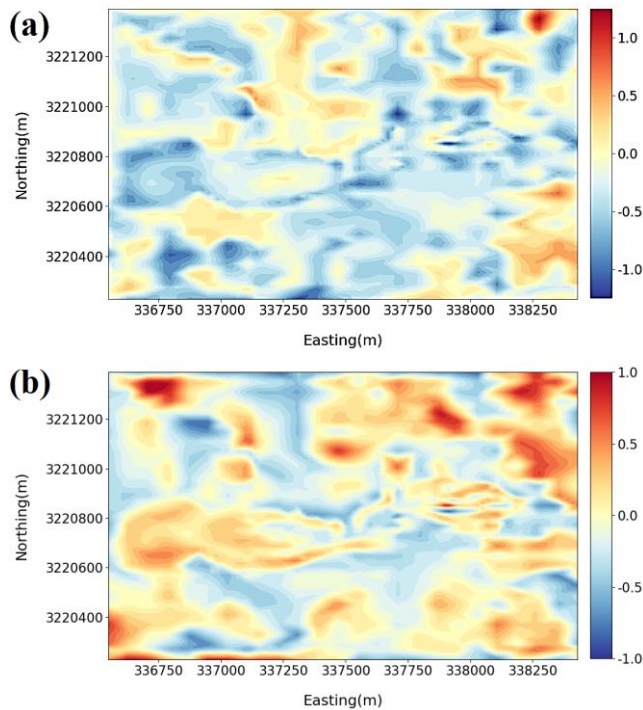
are often located in close proximity, and considering that some regions lack a distinct boundary between them, a multi-stage mineralization process can be inferred for this case study. In the initial stages of deposit formation, low-sulfur magnetite may originate from a relatively sulfur-poor magmatic source. Subsequent hydrothermal events could introduce sulfur-rich fluids into the system, precipitating high-sulfur magnetite and sulfide minerals in structurally controlled zones or along fluid pathways. The spatial distribution of low- and high-sulfur magnetite likely reflects chemical gradients within the hydrothermal system, indicating that different parts of the deposit were exposed to varying sulfur concentrations.
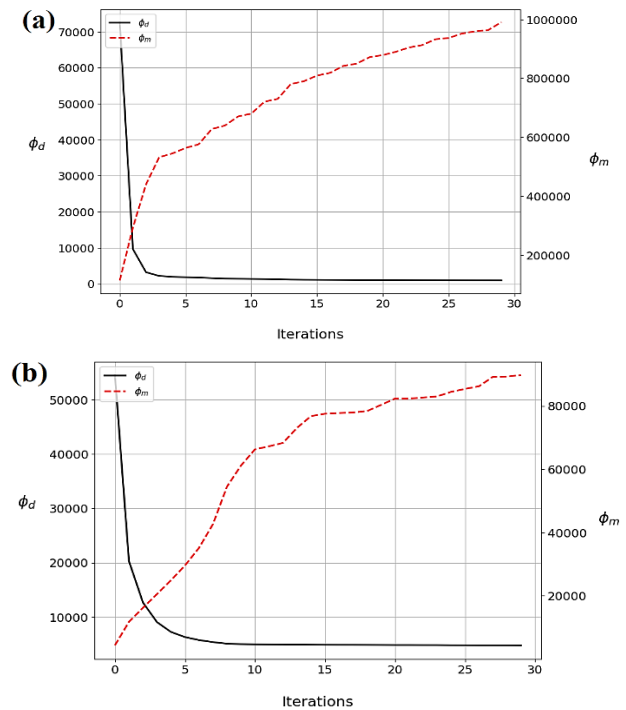

Figure 12. Normalized residuals after sparse norm inversion. (a) Normalized residuals after sparse norm gravity inversion, showing low residuals around the target area. (b) Normalized residuals for magnetic inversion. Although the maximum residual for magnetic inversion is lower than for gravity inversion, near the ore deposits, magnetic inversion shows higher residuals than gravity inversion.

Figure 13. Convergence curves for sparse norm inversion with model norm (ϕ_m) in red and misfit (ϕ_d) in black. (a) Convergence curve for gravity inversion. (b) Convergence curve for magnetic inversion.

Fig. 14 illustrates the 3D models derived from geological findings and inversion outcomes. The geological models (Figs. 14a, 14b, and 14c) are directly derived from samples obtained through extensive drilling operations and exploratory boreholes [45]. In particular, Fig. 14a showcases the rock types prevalent in the study area, which can generally be categorized into two main groups. The first group comprises rocks characterized by a high sulfur magnetite component (HSM), containing pyrite grains that show a distinct schistosity trace. The second group consists of rocks with a low sulfur magnetite component (LSM), rarely containing pyrite grains, and in some cases, cut by quartz veins and chlorite. Notably, the low sulfur component exhibits a considerable correlation with rock formations featuring a high percentage of Fe, as depicted in Fig. 14c. Conversely, the high sulfur component demonstrates alignment with regions exhibiting elevated FeO content, as depicted in Fig. 14b.

Low-sulfur magnetite components are typically associated with primary magmatic processes or early-stage hydrothermal systems that did not introduce significant sulfur. In contrast, high-sulfur magnetite components are often found in zones that have experienced substantial hydrothermal activity, leading to the introduction of sulfur-rich fluids into the ore body. Given that these two primary types of mineralization

To enable a more robust correlation and data interpretation, we have restricted the geological models (Figs. 14a, 14b, and 14c) along the North-South direction (y-axis) to ensure complete overlap with the geophysical models (Figs. 14e and 14d). This aligns the models, creating a consistent comparison area with identical dimensions across both geological and geophysical models. This approach is necessary because the geological data originally covered a broader spatial extent than the geophysical survey area. In Figs. 14d and 14e, we present the 3D models resulting from the inversion process. To facilitate a clearer comparison with the geological models, we applied cutoff values to refine their representation. Specifically, we restricted the density contrast model to the range of 1.2 gr/cm³ -1.5 gr/cm³ and the susceptibility model to the range of 0.8 SI -1.0 SI. This emphasis aims to highlight the more intensely dense and magnetized regions within the models. Additionally, we implemented cutoffs for the Fe and FeO models to delineate rock formations with high Fe and FeO content, enhancing their visibility and relevance within the overall depiction.

Deriving a definitive interpretation and establishing a direct, one-to-one correlation between the geophysical model and the FeO and Fe content models present significant challenges. These challenges stem from the inherent complexity and heterogeneity of the geological setting within our case study. In many instances, distinct boundaries between these elements are not readily discernible due to the intricate geological
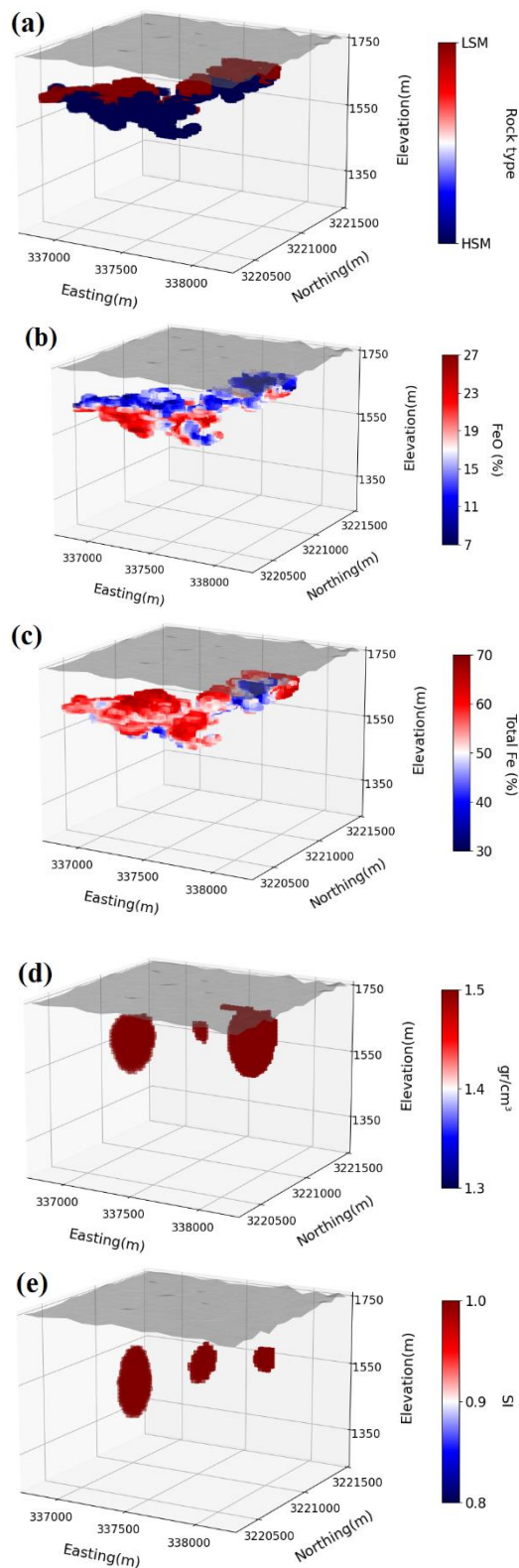
processes at play. Despite these challenges, some general trends emerge from the analysis. The susceptibility models exhibit a stronger correlation with regions characterized by elevated FeO content and high-sulfur magnetite. Conversely, the density contrast model demonstrates a better alignment with areas containing high Fe content and low-sulfur magnetite. These observations suggest a potential link between the geophysical properties and the mineralogical composition of the subsurface. It is important to note that constructing a 3D model grounded in petrological data would provide a more robust foundation for comparison with the geophysical data in future studies.

An examination of the geophysical modelling results presented in Figs. 14d and 14e reveals that both models identify three distinct causative sources. These sources exhibit high-density contrast and significant magnetization. The spatial distribution of the ore bodies in Fig. 14d (density contrast model) overlaps considerably with those in Fig. 14e (magnetic susceptibility model). However, the depth estimations for these causative sources differ between the methods. Fig. 14d indicates a shallower depth for these features compared to Fig. 14e, suggesting a deeper location for the highly magnetized regions. This observation aligns with the information presented in the geological report for the study area and is now confirmed through geophysical modelling [45].

It is important to acknowledge that the presence of diverse rock formations with high density contrast, particularly the metamorphic background, can limit the precision of the gravity method compared to magnetic surveys. Consequently, magnetic methods offer a relatively more accurate approach for targeting ore bodies in this specific geological setting. Nevertheless, both methodologies successfully detected the targeted mineralization, demonstrating the overall effectiveness of integrated geophysical surveys in mineral exploration efforts.

5. Conclusion

In this study, we examined the efficacy of gravity and magnetic inversion from both geophysical and applied perspectives. We first simulated two synthetic models to demonstrate the efficiency of sparse norm gravity and magnetic inversion using tree meshing. This methodology was then applied to the Gol-e-Gohar complex as the real case scenario. Both the density-contrast and susceptibility models showed a low normalized residual, indicating that the inversion algorithm successfully minimized the difference between observed and predicted data. Additionally, we compared these models with true geological models to assess their consistency with total Fe (iron) and FeO (iron oxide) models. The high magnetized regions (0.8-1.0 SI) accurately captured areas with high FeO content with acceptable precision. However, while the density contrast model was less successful than the susceptibility model, it showed an acceptable consistency with both Fe and FeO models as they represent high density contrast. Nevertheless, gravity inversion is not solely dependent on Fe and FeO content, it can detect any rock formation with a high-density contrast, which may not always be economically significant. Finally, we demonstrated that magnetic surveys are more effective in identifying prospect zones in the context of Kiruna-type iron deposits than gravity surveys.

Acknowledgement

Figure 14. 3D geological and geophysical models of the study area. (a) Distribution of the two main rock types (High Sulfur Magnetite Ore and Low Sulfur Magnetite Ore), (b) Distribution of Iron Oxide content (percentage), (c) Distribution of total Iron content (percentage), (d) Density contrast model obtained from sparse norm inversion, (e) Magnetic susceptibility model obtained from sparse norm inversion.

REFERENCES

[1] Nabatian, Gh., Rastad, E., Neubauer, F., Honarmand, M., & Ghaderi, M. (2015). Iron and Fe–Mn mineralisation in Iran: implications for Tethyan metallogeny. Australian Journal of Earth Sciences, 62(2), 211–241. https://doi.org/10.1080/08120099.2015.1002001.

[2] Bialas, T., Bohlen, T., Dannowski, A., Eisenberg-Klein, G., Gassner, L., Gehrmann, R., Heeschen, K., Hölz, S., Jegen, M., Klaucke, I., Krieger, M., Mann, J., Müller, Ch., Prüßmann, J., Schicks, J., Schünemann, E., Schwalenberg, K., Sommer, M., Smilde, P. L., Spangenberg, E., Trappe, H., & Zander, T. (2020). Joint interpretation of geophysical field experiments in the Danube deep-sea fan, Black Sea. Marine and Petroleum Geology, 121, 104551. https://doi.org/10.1016/j.marpetgeo.2020.104551.

[3] Nappi, R., Paoletti, V., D'Antonio, D., Soldovieri, F., Capozzoli, L., Ludeno, G., Porfido, S., & Michetti, A. M. (2021). Joint interpretation of geophysical results and geological observations for detecting buried active faults: The case of the "Il Lago" plain (Pettoranello del Molise, Italy). Remote Sensing, 13(8), 1555. https://doi.org/10.3390/rs13081555.

[4] Marzan, I., Martí, D., Lobo, A., Alcalde, J., Ruiz, M., Alvarez-Marron, J., & Carbonell, R. (2021). Joint interpretation of geophysical data: Applying machine learning to the modeling of an evaporitic sequence in Villar de Cañas (Spain). Engineering Geology, 288, 106126. https://doi.org/10.1016/j.enggeo.2021.106126.

[5] Milano, M., Varfinezhad, R., Bizhani, H., Moghadasi, M., Nejati Kalateh, A., & Baghzendani, H. (2021). Joint interpretation of magnetic and gravity data at the Golgohar mine in Iran. Journal of Applied Geophysics, 195, 104476. https://doi.org/10.1016/j.jappgeo.2021.104476.

[6] Afshar, A., Norouzi, G.-H., Moradzadeh, A., & Riahi, M.-A. (2018). Application of magnetic and gravity methods to the exploration of sodium sulfate deposits: Case study: Garmab mine, Semnan, Iran. Journal of Applied Geophysics, 159, 586-596. https://doi.org/10.1016/j.jappgeo.2018.10.003.

[7] Gonçalves, M. M., & Leite, E. P. (2019). Cooperative inversion of seismic reflection and gravity data: An object-based approach. Journal of Applied Geophysics, 167, 42-50. https://doi.org/10.1016/j.jappgeo.2019.05.006.

[8] Zhdanov, M.S., Tu, X. and Čuma, M. (2022), Cooperative inversion of multiphysics data using joint minimum entropy constraints. Near Surface Geophysics, 20: 623-636. https://doi.org/10.1002/nsg.12203.

[9] Abedi, M. (2022). Cooperative fuzzy-guided focused inversion for unstructured mesh modeling of potential field geophysics: A case study for imaging an oil-trapping structure. Acta Geophysica, 70, 2077–2098. https://doi.org/10.1007/s11600-022-00857-w.

[10] Hu, Y., Wei, X., Wu, X., Sun, J., Huang, Y., & Chen, J. (2024). Three-dimensional cooperative inversion of airborne magnetic and gravity gradient data using deep-learning techniques. GEOPHYSICS, 89(WB67-WB79). https://doi.org/10.1190/geo2023-0225.1.

[11] Gallardo, L. A., & Meju, M. A. (2007). Joint two-dimensional cross-gradient imaging of magnetotelluric and seismic traveltime data for structural and lithological classification. Geophysical Journal International, 169(3), 1261–1272. https://doi.org/10.1111/j.1365-246X.2007.03366.x.

[12] Fregoso, E., & Gallardo, L. A. (2009). Cross-gradients joint 3D inversion with applications to gravity and magnetic data. GEOPHYSICS, 74, L31-L42. https://doi.org/10.1190/1.3119263.

[13] Miotti, F., Zerilli, A., Menezes, P. T. L., Crepaldi, J. L. S., & Viana, A. R. (2018). A new petrophysical joint inversion workflow: Advancing on reservoir's characterization challenges. Interpretation, 6, SG33-SG39. https://doi.org/10.1190/INT-2017-0225.1.

[14] Astic, T., & Oldenburg, D. W. (2019). A framework for petrophysically and geologically guided geophysical inversion using a dynamic Gaussian mixture model prior. Geophysical Journal International, 219(3), 1989–2012. https://doi.org/10.1093/gji/ggz389

[15] Tavakoli, M., Nejati Kalateh, A., Rezaie, M., Gross, L., & Fedi, M. (2021). Sequential joint inversion of gravity and magnetic data via the cross-gradient constraint. Geophysical Prospecting, 69(8), 1542–1559. https://doi.org/10.1111/1365-2478.13120.

[16] Wang, K., & Yang, D. (2023). Joint inversion with petrophysical constraints using indicator functions and the extended alternating direction method of multipliers. GEOPHYSICS, 88, R49-R64. https://doi.org/10.1190/geo2022-0167.1.

[17] Fournier, D., Oldenburg, D., & Davis, K. (2016). Robust and flexible mixed-norm inversion. SEG Technical Program Expanded Abstracts, 2016, 1542-1547. https://doi.org/10.1190/segam2016-13821093.1.

[18] Fournier, D., & Oldenburg, D. W. (2019). Inversion using spatially variable mixed ℓp norms. Geophysical Journal International, 218(1), 268–282. https://doi.org/10.1093/gji/ggz156.

[19] Ardestani, V. E., Fournier, D., & Oldenburg, D. W. (2021). Correction to: Gravity and Magnetic Processing and Inversion Over the Mahallat Geothermal System Using Open Source Resources in Python. Pure and Applied Geophysics, 178, 3289. https://doi.org/10.1007/s00024-021-02805-z.

[20] Ghorbani, M. (2013). The Economic Geology of Iran. Springer Dordrecht. https://doi.org/10.1007/978-94-007-5625-0.

[21] Najmi, F., Malekzadeh Shafaroudi, A., Karimpour, M. H., & Poulson, S. R. (2023). The Bahariyeh iron oxide copper–gold deposit, Khaf-Khashmar-Bardaskan magmatic belt, NE Iran: Constraints from geochemical, fluid inclusions, and O-S isotope studies. Ore Geology Reviews, 159, 105501. https://doi.org/10.1016/j.oregeorev.2023.105501.

[22] Zaremotlagh, S., & Hezarkhani, A. (2016). A geochemical modeling to predict the different concentrations of REE and their hidden patterns using several supervised learning methods: Choghart iron deposit, bafq, Iran. Journal of Geochemical Exploration, 165, 35-48. https://doi.org/10.1016/j.gexplo.2016.02.001. Link to the article

[23] Ziapour, S., Esmaeily, D., Khoshnoodi, K., Niroomand, S., & Simon, A. C. (2021). Mineralogy, geochemistry, and genesis of the Chahgaz (XIVA Anomaly) Kiruna-type iron oxide-apatite (IOA) deposit, Bafq district, Central Iran. Ore Geology Reviews, 128, 103924. https://doi.org/10.1016/j.oregeorev.2020.103924.

[24] Alibabaie, N., Esmaeily, D., Peters, S. T. M., Horn, I., Gerdes, A., Nirooamand, S., Jian, W., Mansouri, T., Tudeshki, H., & Lehmann, B. (2020). Evolution of the Kiruna-type Gol-e-Gohar iron ore district, Sanandaj-Sirjan zone, Iran. Ore Geology Reviews, 127, 103787. https://doi.org/10.1016/j.oregeorev.2020.103787.

[25] Ansari, A., Ghari, H., Alamdar, K., & Moradi, S. (2016). Investigation of the relationship between upward continued

potential fields and depth of the causative bodies: A case study from Gol-Gohar Iron ore mine. Iranian Journal of Geophysics, 5(4), 1-12.

[26] Behnam, S., & Ramazi, H. (2019). Interpretation of geomagnetic data using power spectrum and 3D modeling of Gol-e-Gohar magnetic anomaly. Journal of Applied Geophysics, 171, 103829. https://doi.org/10.1016/j.jappgeo.2019.103829.

[27] Bizhani, H., Mansour Shoar, P., & Moghadasi, M. (2023). 2D Inversion of magnetic and gravity data: a case study on Golgohar mine. International Journal of Mining and Geo-Engineering, 57(1), 41-46. doi: 10.22059/ijmge.2022.342045.594969.

[28] Liu, S., Hu, X., Zhang, H., et al. (2017). 3D Magnetization Vector Inversion of Magnetic Data: Improving and Comparing Methods. Pure and Applied Geophysics, 174, 4421–4444. https://doi.org/10.1007/s00024-017-1654-3.

[29] Shi, X., Geng, H., & Liu, S. (2022). Magnetization Vector Inversion Based on Amplitude and Gradient Constraints. Remote Sensing, 14(21), 5497. https://doi.org/10.3390/rs14215497.

[30] Cockett, R., Kang, S., Heagy, L. J., Pidlisecky, A., & Oldenburg, D. W. (2015). SimPEG: An open source framework for simulation and gradient based parameter estimation in geophysical applications. Computers & Geosciences, 85(Part A), 142-154. https://doi.org/10.1016/j.cageo.2015.09.015.

[31] Zhdanov, M. S. (2015). Inverse theory and applications in geophysics (2nd ed.). Elsevier Science. https://doi.org/10.1016/C2012-0-03334-0.

[32] Nagy, D. (1966). The Gravitational Attraction of a Right Rectangular Prism. GEOPHYSICS, 31, 362-371. https://doi.org/10.1190/1.1439779.[33] Fournier, D. (2019) Advanced potential field data inversion with Lp-norm regularization. PhD Thesis, The University of British Columbia.

[34] Plouff, D. (1976). Gravity and magnetic fields of polygonal prisms and application to magnetic terrain corrections. Geophysics, 41, 727-741.

[35] Sharma, P.V. (1966). Rapid computation of magnetic anomalies and demagnetization effects caused by bodies of arbitrary shape. Pure and Applied Geophysics, 64, 89-109.

[36] Li, Y., & Oldenburg, D.W. (1996). 3-D Inversion of Magnetic Data. Geophysics, 61, 394-408. http://dx.doi.org/10.1190/1.1443968.

[37] Li, Y., & Oldenburg, D. W. (1998). 3-D inversion of gravity data. Geophysics, 63(1), 109-119. http://dx.doi.org/10.1190/1.1444302

[38] Oldenburg, D. W. and Li, Y. (2005) Inversion for applied geophysics: A tutorial. Near-surface geophysics: Society of Exploration Geophysicists, 89-150.

[39] Rezayee, M. H., Khalaj, M., & Mizunaga, H. (2023). Structural analysis and susceptibility inversion based on ground magnetic data to map the chromite mineral resources: A case study of the Koh Safi Chromite Ore Deposit, Parwan, Afghanistan. Geoscience Letters, 10, 43. https://doi.org/10.1186/s40562-023-00298-3.

[40] Alibabaie, N., Esmaeily, D., Peters, S. T. M., Horn, I., Gerdes, A., Nirooamand, S., Jian, W., Mansouri, T., Tudeshki, H., & Lehmann, B. (2020). Evolution of the Kiruna-type Gol-e-Gohar iron ore district, Sanandaj-Sirjan zone, Iran. Ore Geology Reviews, 127, 103787. https://doi.org/10.1016/j.oregeorev.2020.103787.

[41] Berberian, M., & King, G. (1981). Towards a paleogeography and tectonic evolution of Iran. Canadian Journal of Earth Sciences, 18(2), 210-265. https://doi.org/10.1139/e81-019.

[42] Babaki, A., & Aftabi, A. (2006). Investigation on the model of iron mineralization at Gol Gohar iron deposit, Sirjan-Kerman. Geosciences, 16 (61), 40-59. SID. https://sid.ir/paper/31412/en

[43] Badavi, M., Atapour, H., & Mohammadi, M. (2019). Mineralogy, petrography, geochemistry of magnetite ore and sulfide minerals and the possible model of mineralization at Anomaly 3, Gol-e-Gohar, iron mine, Sirjan (Kerman). Petrology, 38, 49–79. (In Persian with English Abstract).

[44] Bayati-Rad, Y., Mirnejad, H., & Ghalamghash, J. (2013). Distribution and abundance of rare earth elements in magnetite from Gol-Gohar iron ore deposit, Sirjan-Kerman. Scientific Quarterly Journal of Geosciences, 23(90), 217–224.

[45] Iran Minerals Production and Supply Company (IMPASCO). (2017). Mineral reserve estimation report for Gol Gohar Sirjan, mine 2.

[46] Beltrão, J. F., Silva, J. B. C., & Costa, J. C. (1991). Robust polynomial fitting method for regional gravity estimation. GEOPHYSICS, 56, 80-89. https://doi.org/10.1190/1.1442960.